Eddy-induced Chlorophyll-a Variations in the Northern Indian Ocean: A Study Using Multi-Source Satellite Data and Deep Learning

Yingjie Liu[1], Xiaofeng Li[1]

5 [1]CAS Key Laboratory of Ocean Circulation and Waves, Institute of Oceanology, Chinese Academy of Sciences, Qingdao 266071, China.

Correspondence to: Xiaofeng Li (lixf@qdio.ac.cn)

Abstract. Mesoscale eddies, including surface-intensified eddies (SEs) and subsurface-intensified eddies (SSEs), significantly influence phytoplankton distribution in the ocean. Nevertheless, due to the sparse in-situ data, it is still unclear
10 in understanding the characteristics of SSEs and their influence on chlorophyll-a (Chl-a) concentration. Consequently, the study utilized a deep learning model to extract SEs and SSEs in the North Indian Ocean (NIO) from 2000 to 2015, using long time series of satellite-derived sea surface height (SSH) and sea surface temperature (SST) data. The analysis revealed that SSEs accounted for 44% of the total eddies in the NIO, and their SST signatures exhibited an opposite behavior compared to SEs. Furthermore, by integrating ocean color remote sensing data, the study investigated the contrasting
15 impacts of SEs and SSEs on Chl-a concentration in two basins of the NIO: the Arabian Sea (AS) and the Bay of Bengal (BoB), known for their disparate biological productivity. In the AS, SEs induced Chl-a anomalies that were two to three times higher than those caused by SSEs. Notably, there were no significant differences in Chl-a anomalies induced by the same type of eddies between summer and winter. In contrast, the BoB exhibited distinct seasonal variations, where SEs induced slightly higher Chl-a anomalies than SSEs during the summer, while substantial differences were observed during
20 the winter. Specifically, subsurface-intensified anticyclonic eddies (SSAEs) led to positive Chl-a anomalies, contrasting the negative anomalies induced by surface-intensified anticyclonic eddies (SAEs) with comparable magnitudes. Moreover, while both subsurface-intensified cyclonic eddies (SSCEs) and surface-intensified cyclonic eddies (SCEs) resulted in positive Chl-a anomalies, the magnitude of SSCEs was only one-fourth of that induced by SCEs. The distinct Chl-a anomalies between SEs and SSEs can be attributed to the contrasting subsurface structures revealed by Argo profiles. The upward displacement
25 of isopycnals within SSAEs and the downward displacement within SSCEs in the upper 30-50 meters lead to higher and lower Chl-a concentrations, respectively. The study provides a valuable approach to investigating subsurface eddies and contributes to a comprehensive understanding of their influence on chlorophyll concentration.

1 Introduction

Mesoscale eddies significantly influence phytoplankton distribution through several processes, including eddy stirring
(Chelton et al., 2011b), eddy trapping (Lehahn et al., 2011); eddy upwelling and downwelling (Gaube et al., 2013); eddy-
induced Ekman pumping (Gaube et al., 2014; Siegel et al., 2011; Gaube et al., 2013), and eddy strain-induced pumping
(Zhang et al., 2019). Previous studies predominantly focused on investigating chlorophyll distribution induced by surface-
intensified eddies (SEs), which can be generally classified into surface-intensified anticyclonic eddies (SAEs) and surface-
intensified cyclonic eddies (SCEs) based on their rotation direction (Chen et al., 2019). It is important to note that mesoscale
eddies can be further subdivided into distinct categories by the location of their core, where the potential vorticity reaches its
maximum. The core can be located in the surface or subsurface layers (Assassi et al., 2016), resulting in SEs or subsurface-
intensified eddies (SSEs). SSEs have been observed in various ocean regions using in-situ data (Zhang et al., 2017;
Bashmachnikov et al., 2014; Bashmachnikov et al., 2013; Chaigneau et al., 2011; Morales et al., 2012). However, the sparse
availability of in-situ data makes it challenging to determine whether the eddies observed in satellite-derived maps are
subsurface-intensified. Therefore, there is still uncertainty for further research regarding the characteristics of SSEs and their
impact on chlorophyll concentration.

The surface and interior ocean are highly correlated, and the subsurface signals in the ocean can be reflected at the surface
(Klemas and Yan, 2014). The relationship between sea surface height (SSH) and sea surface temperature (SST) within
eddies has proven to be an effective index for differentiating between SEs and SSEs using multi-source remote sensing data
(Assassi et al., 2016; Bashmachnikov et al., 2013; Caballero et al., 2008), which has demonstrated successful application
across diverse oceanic regions (Wang et al., 2019; Greaser et al., 2020; Trott et al., 2019). However, SST and SSH within
eddies are subject to the intricate influence of multiple physical processes, leading to the intricate and nonlinear SST-SSH
relationship that traditional statistical methods may not adequately capture. The deep learning (DL) technique has recently
demonstrated remarkable capabilities in analyzing and extracting intricate patterns and relationships from multi-source big
data (Ham et al., 2019; Lecun et al., 2015; Lu et al., 2019; Su et al., 2015; Jiang et al., 2022; Su et al., 2021), enabling a
deeper and more comprehensive exploration of the intricate dynamics within SEs and SSEs.

Mesoscale eddies are prominent features in the Northern Indian Ocean (NIO) (Zhan et al., 2020; Trott et al., 2019; Chen et
al., 2012; Gulakaram et al., 2020; Greaser et al., 2020), which consists of the Bay of Bengal (BoB) and the Arabian Sea (AS),
two distinct basins that exhibit substantial differences in terms of their biological productivity. In the NIO, intense
southwesterly summer monsoon winds blow between June and September, while relatively weak northeasterly winter winds
blow between November and February (Prasad, 2004). Besides, the winds over the AS are stronger than the BoB due to the
Findlater Jet during the summer monsoon (Findlater, 1969). The intense summer monsoon makes the AS one of the world's
most productive regions (Kumar et al., 2002), with various physical processes contributing to its productivity, such as open
ocean upwelling (Brock et al., 1991), wind-driven mixing (Lee et al., 2000), lateral advection (Kumar et al., 2001), and the
coastal upwelling along Somalia (Kumar et al., 2002). Conversely, the BoB is regarded as a region with lower biological

productivity due to weaker summer monsoon and lower salinity (Kumar et al., 2002; Prasad, 2004). Previous literature mainly investigates the influence of SEs on biological features in the AS and the BoB (Yang et al., 2020; Shafeeque et al., 2021; Smitha et al., 2022). Further investigations are needed to examine the effects of SSEs on chlorophyll distribution in the NIO.

65   Therefore, the study proposes a DL-based model to distinguish between SEs and SSEs using satellite-derived altimetry SSH and infrared SST data. Consequently, the study conducts a comparative analysis to assess the differential impacts of SEs and SSEs on chlorophyll concentrations in the NIO. Section 2 introduces the satellite-derived data, in-situ data, and methods to distinguish and analyze SEs and SSEs. Section 3 examines and contrasts the spatial characteristics and seasonal variations of SST and chlorophyll anomalies caused by SEs and SSEs in the AS and the BoB. Section 4 of the study focuses

70   on constructing subsurface eddy structures using in-situ data to validate the DL-based model's accuracy and explain the differences in chlorophyll distribution caused by SEs and SSEs. In Section 5, the study presents its conclusions based on the findings and analysis conducted throughout the research.

2 Data and Methods

2.1 Data

75 #### 2.1.1 Satellite-derived Dataset and Products

The SSH anomalies (SSHA) dataset is obtained from the European Copernicus Marine Environment Monitoring Service (Pujol et al., 2016). The dataset is derived by combining data from multiple altimeter missions and is available daily. The spatial resolution of the dataset is 0.25°, providing detailed information about the variations in SSH across the study region. A spatial filter with half-power filter cutoffs of 20° longitude by 10° latitude is applied to the SSHA map to facilitate the

80   detection of eddies (Chelton et al., 2011a). The SST dataset used in the study is the NOAA Optimum Interpolation (OI) SST product from Reynolds et al. (2007). The dataset is available daily and has a spatial resolution of 0.25°. To identify eddy‐induced SST anomalies (SSTA), temporal and spatial filters were applied to the SST field. The temporal filter utilized a band-pass Butterworth window to preserve the temporal signal within 7-90 days. The filter is chosen based on the typical lifetimes of eddies in the NIO, ensuring that the relevant temporal variations associated with eddy dynamics are captured.

85   Meanwhile, the spatial filter employed a moving average Hann window to retain spatial scales smaller than 600 km. These filters have been shown to provide robust results for obtaining mesoscale SSTA field (Bôas et al., 2015).

In addition, the ocean color observed chlorophyll-a (Chl-a) product is used to evaluate chlorophyll concentrations induced by eddies. The daily Chl-a dataset of 4 km was produced by the European Space Agency (Maritorena et al., 2010). The Chl-a measurements were averaged onto the 0.25°grid as the SSHA observations. The unit for Chl-a concentration is mg/m^3, and

90   Chl-a values are firstly log-transformed due to their lognormal distribution. In order to obtain eddy-induced Chl-a anomalies (Chl-a'), the satellite log-transformed Chl-a field was first filtered with a 7-90 day Butterworth time filter. The time-filtered

Chl-a field was then anti-log-transformed to get the original units of mg/m^3 for direct comparisons of their results inside eddies (Gaube et al., 2013). Finally, a 600 km high-pass spatial filter was applied to the time-filtered Chl-a field, generating an eddy-induced Chl-a' field.

2.1.2 In-situ Data

The study utilizes Argo profiles to construct the subsurface eddy structures. The Argo floats provide temperature and salinity measurements from the sea surface to thousands of meters below, allowing for a comprehensive understanding of subsurface conditions. Besides, the daily climatology of subsurface temperature and salinity values is acquired from the CSIRO Atlas of Regional Seas 2009 (CARS09) product. These climatological values are then subtracted from the Argo profiles, enabling the isolation of anomalies specific to the eddy features.

2.2 Methods

2.2.1 DL-based Eddy Identification Model

The study aims to extract SEs and SSEs based on the differences in their thermodynamic structures. Fig. 1a illustrates the shape of isopycnal levels for SEs and SSEs, as described by Assassi et al. (2016). SAEs exhibit positive SSHA and the deepening of isopycnals, resulting in negative sea surface density (SSρ) anomalies. Conversely, SCEs show negative SSHA and the upward displacement of isopycnals, inducing positive anomalies in SSρ. Therefore, both SCEs and SAEs show negative relationships between SSρ and SSHA. For SSEs, the scenario is slightly different. Subsurface-intensified AEs (SSAEs) also exhibit positive SSHA, similar to SAEs. However, the shape of isopycnal levels associated with SSAEs is lens-like, indicating an upward displacement of water above the center and a downward displacement below it. Similarly, subsurface-intensified CEs (SSCEs) maintain negative SSHA, as observed in SCEs. However, the isopycnal levels above SSCEs exhibit a depressed shape, indicating a downward displacement of water, while the isopycnals below the SSCEs display a domed shape, indicating an upward displacement. Consequently, the SSρ anomalies within SSEs have the opposite sign compared to SEs, leading to a positive SSρ/SSHA ratio for both SSAEs and SSCEs. Therefore, the sign of SSρ/SSHA can be used as an indicator to distinguish SAEs and SSAEs, or SCEs and SSCEs. However, it is important to note that SSρ cannot be directly measured from remote sensing observations. Instead, at first order, SSρ are primarily influenced by SST variations, which can be observed remotely. Thus, the SSTA-SSHA relationship within eddies can be employed to differentiate between SEs and SSEs.

Accordingly, a DL-based model is developed to distinguish between SEs and SSEs by integrating satellite-derived SSHA and SSTA data mentioned in section 2.1.1. As shown in Fig. 1b, the DL-based model employs an encoder-decoder architecture (Ronneberger et al., 2015) for feature extraction from SSHA and SSTA data. The encoder-decoder architecture offers several advantages in terms of simplicity, reduced training time, fewer parameters, and lower sample requirements. Consequently, it effectively reduces computational complexity while efficiently extracting features. In the encoder part of

the model, convolutions are utilized to extract spatial information from the input image, followed by max-pooling to reduce the feature dimensions progressively. In the decoder part, up-convolutions are employed to restore object details and spatial
125   information. Besides, features from the corresponding encoder and decoder layers are concatenated to enrich the decoded information. Especially to address the complex nonlinear relationship between SSHA and SSTA within mesoscale eddies, a dense connection network (Dolz et al., 2018) is incorporated into the encoder part to facilitate the fusion of remote sensing SSHA and SSTA data. Unlike traditional convolutional neural networks, where information flows sequentially from one layer to the next, the dense connection network establishes direct connections from any layer to all subsequent layers in a
130   forward manner. The forward propagation is represented by Eq. (1):

$$x_l^s = H_l^s([x_{l-1}^1, x_{l-1}^2, x_{l-2}^1, x_{l-2}^2, \cdots, x_0^1, x_0^2]), \qquad\qquad (1)$$

where x represents a single network layer, the superscript s denotes the modality of the network layer, and the subscript l indicates the layer number. The function H_l^s represents a composite operation that includes batch normalization (BN), rectified linear unit (ReLU), and convolutional operations. By incorporating dense connections, the DL-based model
135   introduces implicit deep supervision, enhancing learning capabilities and improving information flow and gradient throughout the model. It not only facilitates the extraction of correlated spatiotemporal features of SSHA and SSTA at different scales but also mitigates the issue of gradient vanishing that commonly arises with increasing network depth. Consequently, the proposed model ensures a more efficient and accurate training process.

The DL-based eddy identification model was trained and validated using datasets generated by a traditional SSH-based
140   method (Liu et al., 2016; Chelton et al., 2011a), which extracts AEs and CEs by searching closed SSHA contours. Then, to determine whether an AE is SAE or SSAE and a CE is SCE or SSCE, the study calculates the mean SSTA within one radius within eddies. The mean SSTA within SCEs and SSAEs is negative, while positive within SAEs and SSCEs. As a result, we obtained the training dataset consisting of 1827 samples from 2000-2004 and the testing dataset consisting of 365 samples from 2005. Each sample contains four kinds of eddies in the NIO: SSCEs, SCEs, SAEs, and SSAEs, with pixels labeled as
145   '1', '2', '3', and '4', respectively. The study utilized the dice loss function to optimize the DL-based eddy identification model. When the model was evaluated on the testing samples, it achieved a loss of approximately 0.12 and an accuracy of around 0.95 (Figs. 1c-d). With a low loss value and a high accuracy rate, the DL-based model demonstrated promising results in accurately identifying and classifying the different types of eddies in the testing samples (Fig. 1e).

2.2.2 Surface and Subsurface Composite Analysis over Eddies

150   The study conducted a surface composite analysis combining eddy-induced SSTA and Chl-a' data on a normalized grid. The analysis aims to examine the composite patterns of SSTA and Chl-a' associated with different types of eddies. The eddy-induced SSTA and Chl-a' values within a region twice the radius (R) of each eddy were collected to construct the surface composite analysis. These values were then interpolated onto a normalized circle of the same size, as depicted in Fig. 2a. Next, composite SSTA and Chl-a' maps were generated by averaging the normalized anomaly fields over the eddies of the

155   same type. This process involved grouping the eddies based on their characteristics and calculating the average SSTA and Chl-a' values at each grid point within the normalized circle for each group of eddies.

To analyze the characteristics of eddies' subsurface structures, we select Argo profiles co-located within 1.5 R from the eddy core to construct the 3D structure of mesoscale eddies. Quality control was first applied to eddy-collocated Argo floats using the following criteria: (1) Only profiles data flagged as good quality were considered; (2) each Argo profile must

160   contain a data point at a depth of 10 m or less, and at least one data point at a depth of 1,000 m or greater; (3) there are more than 30 observations between 0 m and 1,000 m. Secondly, temperature and salinity data were interpolated on a regular 10 m grid ranging from 10 m to 1,000 m because Argo floats may or may not have observed data at the surface. Thirdly, the Argo profiles were processed by subtracting the CARS09 dataset to obtain temperature and salinity anomalies, specifically within the eddy regions. Moreover, potential density anomalies were calculated by temperature and salinity anomalies according to

165   the International Thermodynamic Equation of Seawater (Mcdougall and Barker, 2011). Subsequently, the temperature and potential density anomalies within 1.5R of mesoscale eddies were interpolated into 0.1R × 0.1R × 10 m grid points up to a horizontal distance of 1.5R (Fig. 2b) by the inversed distance weighting interpolation method (Bartier and Keller, 1996).

3 Results

3.1 Case Studies of SST and Chl-a within SEs and SSEs

170   The study conducts case studies to preliminarily examine characteristics of SSTA and Chl-a' within SEs and SSEs. As shown in Fig. 3a, the DL-based model detected an SAE and an SCE on the AS's west coast on February 2, 2005. The SAE displays positive signatures in SSTA images, indicating warm water, and negative signatures in Chl-a' images, indicating lower Chl-a concentrations. In contrast, the SCE shows negative SSTA and positive Chl-a' signatures. These findings are consistent with conventional knowledge, where AEs are generally identified as warm rings with lower Chl-a concentrations in ocean color

175   maps, while CEs exhibit the opposite pattern (Gaube et al., 2014; Hsu et al., 2016). Fig. 3b shows an example of an SSAE on the east coast of the AS on March 13, 2002. The SSAE is associated with cold water and displays positive Chl-a' signatures, indicating higher Chl-a concentrations. Similarly, Fig. 3c presents an example of an SSCE in the North Central BoB on November 28, 2014. The SSCE is associated with positive SSTA, indicating warm water, but exhibits negative Chl-a' values, indicating lower chlorophyll-a concentrations. The above findings suggest that SSEs exhibit distinct effects on Chl-a

180   concentrations compared to SEs.

3.2 Spatial Distribution of SST and Chl-a within SEs and SSEs

The study applied the DL-based model to identify SEs and SSEs in the NIO from 2000 to 2015. As a result, 62,688 SAEs, 49,573 SSAEs, 72,807 SCEs, and 57,620 SSCEs are observed. The number represents the aggregate count of eddies of identical type across all eddy snapshots during 2000-2015. Figs. 4a-d depict the spatial distribution of eddy concentration,

185   representing eddy numbers of the same type observed within a 1°×1° grid during 2000-2015. In the NIO, the number of SEs
       (SAEs and SCEs) accounted for 56% of the total, while SSEs (SSAEs and SSCEs) constituted 44%.

       The coastal areas of the Arabian Peninsula and the East Indian Coastal Current (EICC) in the BoB exhibited a pronounced
       abundance and prevalence of SEs and SSEs. These regions are known for their active eddy generation mechanisms,
       including coastal upwelling, Rossby waves, and barotropic instabilities in the AS (Trott et al., 2018; Zhan et al., 2020), as
190   well as monsoon conversion, EICC instability, and westward Rossby wave energy transmission in the BoB (Somayajulu et
       al., 2003; Chen et al., 2012; Cheng et al., 2018; Cui et al., 2016). Figs. 4e-h display the spatial distributions of eddy-induced
       SSTA averaged within a 1°×1° grid. SAEs and SSCEs exhibit positive SSTA values (Figs. 4e, 4h), indicating warmer water,
       while SSAEs and SCEs display negative SSTA values (Figs. 4f, 4g), indicating cooler water. The distinct SSTA signatures
       exhibited by these eddies align with the expected patterns associated with SEs and SSEs defined in section 2.2.1.

195   Fig. 5 illustrates the spatial distribution of Chl-a' averaged within a 1°×1° grid, specifically induced by SEs and SSEs in
       the NIO during 2000-2015. Chl-a' induced by SAEs (Fig. 5a) exhibits predominantly negative values across most areas of
       both basins. The western parts of both basins, particularly in the Somali Current (SC) region in the AS, exhibit the lowest
       concentrations of Chl-a'. It suggests that SAEs are associated with decreased phytoplankton biomass or lower productivity in
       these regions. Whereas, Chl-a' induced by SSAEs (Fig. 5b) shows predominantly positive signals in more areas, with a
200   concentration observed along the northeastern coasts of both basins, which indicates that SSAEs are associated with higher
       productivity in these regions. For SCEs (Fig. 5c), eddy-induced Chl-a' exhibits positive values and a higher concentration
       along the SC region. In contrast, in most areas, Chl-a' induced by SSCEs (Fig. 5d) is generally insignificant. It shows
       negative values in the Gulf of Aden and north of the Andaman Sea. It implies that SSCEs may have less effect on primary
       productivity in these regions than SCEs.

205   **3.3 Seasonal Variations of Composite SST and Chl-a within SEs and SSEs**

       Considering distinct monsoon and productivity backgrounds in the AS and the BoB regions, we conducted a composite
       analysis of SSTA and Chl-a' within SAEs, SSAEs, SCEs, and SSCEs in summer and winter monsoons for both basins. Fig. 6
       shows composite SSTA over SEs and SSEs in the AS and the BoB during summer and winter monsoons. In both basins,
       composite SSTA over the SEs and SSEs exhibit similar monopole patterns with opposite signals. Specifically, the composite
210   SSTA signals for SAEs were positive, while those for SCEs were negative. Conversely, the signals for SSAEs were positive,
       and SSCEs displayed negative SSTA patterns. Despite the opposite SSTA signals between the SEs and SSEs, their
       magnitudes were comparable within the same season, indicating that the inversed SSTA signal within SSEs should not be
       overlooked.

       In addition, eddy-induced SSTA over both SEs and SSEs are more pronounced during summer compared to winter in the
215   AS (Figs. 6a-h). Table 1 shows that composite SSTA extremums within SEs and SSEs during summer are at least 1.6
       times higher than those observed during winter. The seasonal variation in the intensity of monsoon winds is suggested to
       influence the impact of eddy-induced SSTA in the AS throughout the year. The intensified southwesterly winds during the

summer monsoon contribute to enhanced upwelling and mixing processes, leading to greater changes in SSTA induced by eddies. In contrast, the weaker northeasterly winds during the winter monsoon are associated with reduced upwelling and

220 mixing, leading to relatively less pronounced eddy-induced SSTA. However, composite SSTA over the SEs and SSEs did not exhibit a significant seasonal variation in the BoB. The intensities of eddy-induced SSTA were slightly larger during the summer monsoon than in winter, with a difference of 0.1°C (Table 1). The observed slight difference in intensity of composite eddy-induced SSTA between the BoB and the AS can be primarily attributed to the seasonal variations in monsoon winds. The BoB exhibits a less pronounced seasonal variation in monsoon winds than the AS. During the summer

225 monsoon, the AS experiences stronger winds than the BoB, while both basins encounter relatively weaker winds during the winter monsoon. The divergence in wind strength contributes significantly to the distinct intensity of eddy-induced SSTA between the two basins.

Despite the opposing signals of SSTA induced by SEs and SSEs, they generally exhibit a consistent signal in terms of Chl-a' (Fig. 7). In the AS, composite Chl-a' shows dipole patterns with positive signals for SAEs and SSAEs and negative

230 signals for SCEs and SSCEs (Figs. 7a-h). Although the Chl-a' signals within the SEs and SSEs exhibit similar patterns, their magnitudes significantly differ. According to the data presented in Table 1, the Chl-a' induced by SAEs during summer and winter are -0.040 mg/m³ and -0.048 mg/m³, respectively. Conversely, the Chl-a' induced by SSAEs during summer and winter are -0.019 mg/m³ and -0.017 mg/m³, respectively. It indicates that the Chl-a concentration within SAEs is notably lower than SSAEs, with approximately half of the concentration observed in the latter. On the other hand, the Chl-a

235 concentration within SCEs is two to three times higher compared to SSCEs. Specifically, the Chl-a' induced by SCEs during summer and winter is 0.074 mg/m³ and 0.084 mg/m³, respectively, whereas the Chl-a' induced by SSCEs during summer and winter is 0.019 mg/m³ and 0.040 mg/m³, respectively. Notably, Chl-a' intensities over both SEs and SSEs in the AS demonstrate a relatively consistent pattern between the summer and winter monsoons, with no significant variation observed. Winter productivity in the AS has been suggested to be comparable to, or occasionally even surpass, that of the summer

240 (Piontkovski et al., 2011). The enhanced productivity during winter is attributed to the convective winter mixing, which facilitates the upward transport of nutrients to the surface layer (Banse and English, 2000).

However, significant seasonal variations are observed in the impact of SEs and SSEs on Chl-a concentration in the BoB (Figs. 7i-p). During the summer monsoon, eddy-induced Chl-a' over the SEs and SSEs exhibit similar patterns (Figs. 7i-l), with slight differences in magnitudes (±0.006 mg/m³). As shown in Table 1, the Chl-a' induced by SAEs and SSAEs are -

245 0.029 mg/m³ and -0.023 mg/m³, indicating a decrease in chlorophyll concentration compared to the surrounding areas. On the other hand, SCEs and SSCEs exhibit positive Chl-a' values of 0.022 mg/m³ and 0.016 mg/m³, respectively, indicating an increase in chlorophyll concentration. During the winter monsoon, composite Chl-a' induced by SEs and SSEs exhibit distinct patterns (Figs. 7m-p). Specifically, SAEs exhibit a predominant presence of negative Chl-a' values, with a minimum concentration of -0.018 mg/m³. In contrast, SSAEs are characterized by positive Chl-a' values, reaching a maximum

250 concentration of 0.022 mg/m³. Besides, SCEs predominantly exhibit positive Chl-a' values, with a maximum concentration of 0.033 mg/m³, which is approximately four times higher than that induced by SSCEs. Additionally, the concentration of

eddy-induced Chl-a' in the BoB was considerably lower than in the AS. The lower Chl-a concentration within eddies in the BoB is attributed to weakened vertical mixing resulting from freshwater-induced stratification and relatively weaker winds (Prasanna Kumar et al., 2002).

4 Discussion

Relying solely on the SSHA-SSTA relationship may lead to potential misidentification of SSEs due to various sources of errors (Assassi et al., 2016). For example, it is challenging when dealing with eddies exhibiting multicore structures of similar strength, making it difficult to accurately determine the most intense core's location. Besides, in regions where salinity plays a significant role in stratification, variations of SSρ may not be dominated by SST variations at first order. In order to validate the accuracy and robustness of the DL-based eddy identification model, the study employs quality-controlled Argo profiles to construct subsurface eddy structures for both SEs and SSEs in the AS and the BoB. During 2000-2015, the numbers of Argo profiles within SAEs, SSAEs, SCEs, and SSCEs were as follows: 2448, 2127, 3097, and 1852 profiles in the AS, and 863, 1341, 1070, and 830 profiles in the BoB, respectively.

Fig. 8 provides insights into the subsurface temperature anomalies within SEs (SAEs and SCEs) and SSEs (SSAEs and SSCEs) in the AS and the BoB. In the AS, SAEs and SCEs exhibit positive and negative temperature anomalies throughout the structure, with maximum temperature anomalies at approximately 100 m (Figs. 8a, c). Conversely, SSAEs and SSCEs display negative and positive temperature anomalies in the upper 30 m, contrasting with their subsurface layers (Figs. 8b, d). Similar differences in the subsurface temperature structure between SEs and SSEs are also observed in the BoB (Figs. 8e-h). Furthermore, SSCEs exhibit positive temperature anomalies extending to 50 m and show cold cores between 50 -300 m (Fig. 8h). The vertical temperature structure aligns with previous studies that have identified SSCEs with cold cores between 50 and 300 m using CTD data in the BoB (Babu et al., 1991).

Furthermore, the study constructs vertical structures of potential density within the eddies (Fig. 9) to determine whether the isopycnal displacements of SEs and SSEs align with the definition proposed by Assassi et al. (2016). In the AS, SAEs and SCEs exhibit negative and positive potential density anomalies throughout the structure, respectively (Figs. 9a, c). However, SSAEs and SSCEs show a small cap of positive and negative potential density anomalies, respectively, above 30 m, contrasting with their subsurface layers (Figs. 9b, d). Similar patterns are observed in the BoB, where SSAEs display positive potential density anomalies within the upper 30 m (Fig. 9f). In comparison, SSCEs show negative potential density anomalies within the upper 50 m (Fig. 9h). Thus, SSAEs generally exhibit positive potential density anomalies in the near-surface layer, which can be attributed to the upward displacement of isopycnals. In contrast, SSCEs show negative potential density anomalies due to downward displacement. These findings align well with the schematic diagram of isopycnal displacements of SEs and SSEs depicted in Fig. 1a.

By reconstructing the subsurface structure of eddies, the study confirms the accuracy of the DL-based model in distinguishing between SEs and SSEs. Additionally, distinct displacements of isopycnals between SEs and SSEs provide

insight into the contrasting impacts on Chl-a distribution. The upward movement of isopycnals within SSAEs leads to the
285   ascent of deeper water to the surface layer. This process facilitates the vertical transport of nutrients, promoting enhanced
biological productivity and higher concentrations of Chl-a within SSAEs than SAEs. The vertical movement of water masses
and the associated nutrient supply contribute to the favorable conditions for phytoplankton growth and the accumulation of
Chl-a in SSAEs. Similarly, the downward displacement of isopycnals within SSCEs leads to the subduction of surface water,
resulting in lower Chl-a concentrations compared to SCEs.

290   **5 Conclusions**

The study proposes a DL-based model that integrates satellite-derived SSH and SST data to
accurately distinguish between SEs and SSEs in the NIO during 2000-2015. In the NIO, the number of SEs (SAEs and SCEs)
accounted for 56% of the total, while SSEs (SSAEs and SSCEs) constituted 44%. SAEs and SCEs exhibit positive and
negative SSTA, contrary to SSAEs and SSCEs, respectively. In addition, SEs and SSEs show significant differences in
295   spatial characteristics and composite patterns of eddy-induced Chl-a. On the one hand, SAEs (SCEs) induce negative
(positive) anomalies in Chl-a concentration, with the most significant effects observed in the Somali Current region.
However, SSAEs cause positive Chl-a anomalies along the northeastern coast of both basins, while SSCEs lead to negative
Chl-a anomalies in the Gulf of Aden and the northern part of the Andaman Sea. On the other hand, composite Chl-a within
SAEs are considerably lower compared to SSAEs, which is about twice times lower in the latter. In contrast, the Chl-a
300   concentration in SCEs is twice or three times higher than in the SSCEs.

The distinct subsurface structures between SEs and SSEs provide insight into the contrasting impacts on Chl-a distribution.
SAEs and SCEs exhibit negative and positive potential density anomalies throughout the structure. However, SSAEs exhibit
positive potential density anomalies in the upper 30 -50 m, which can be attributed to the upward displacement of isopycnals.
The upward movement facilitated the transport of deeper water to the surface layer, inducing higher Chl-a concentrations
305   within SSAEs. Besides, SSCEs show negative potential density anomalies in the upper 30 -50 m due to the downward
displacement of isopycnals, leading to lower Chl-a concentrations than SCEs. In conclusion, the study demonstrates the
effectiveness of the DL-based model in distinguishing between SEs and SSEs by fusing remote sensing SSH and SST data.
By applying the model, the study enhances the comprehension of the impacts of SSEs on Chl-a distribution and contributes
to a deeper understanding of the complex interactions between eddy dynamics and biogeochemical processes.

310   **Data availability**

All data used in the analysis are available in public repositories. The SSHA dataset is available at
https://doi.org/10.48670/moi-00148.   OISST   product   can   be   downloaded   from
https://psl.noaa.gov/data/gridded/data.noaa.oisst.v2.highres.html.   The   Chl-a   data   were   downloaded   from

315 http://www.globcolour.info. Argo data can be downloaded from http://www.coriolis.eu.org. CARS2009 data was obtained from http://www.marine.csiro.au/~dunn/cars2009/. The DL-based model and eddy dataset used in this paper will eventually be deposited by the time the article is accepted.

Author contributions

Yingjie Liu and Xiaofeng Li: writing, analysis, and revision. All authors provided feedback on the analysis and interpretation of results and contributed to reviewing and editing the manuscript. All authors have read and agreed to the published version
320 of the manuscript.

Competing interests

The authors declare that they have no conflict of interest.

Acknowledgments

This work was supported by the Qingdao National Laboratory for Marine Science and Technology, the special fund of
325 Shandong province (No. LSKJ202204302), the Natural Science Foundation of Shandong Province (ZR2020MD083), the National Natural Science Foundation of China (U2006211), the Strategic Priority Research Program of the Chinese Academy of Sciences (XDA19060101, and XDB42000000), Major scientific and technological innovation projects of Shandong Province (2019JZZY010102), and the CAS Program (Y9KY04101L).

References

330 Assassi, C., Morel, Y., Vandermeirsch, F., Chaigneau, A., Pegliasco, C., Morrow, R., Colas, F., Fleury, S., Carton, X., and Klein, P.: An index to distinguish surface-and subsurface-intensified vortices from surface observations, J. Phys. Oceanogr., 46, 2529-2552, doi: 10.1175/JPO-D-15-0122.1, 2016.
Babu, M. T., Kumar, S. P., and Rao, D. P.: A subsurface cyclonic eddy in the Bay of Bengal, J. Mar. Res., 49, 403-410, doi: 10.1357/002224091784995846, 1991.
335 Banse, K. and English, D.: Geographical differences in seasonality of CZCS-derived phytoplankton pigment in the Arabian Sea for 1978–1986, Deep Sea Research Part II: Topical Studies in Oceanography, 47, 1623-1677, doi: 10.1016/S0967-0645(99)00157-5, 2000.
Bartier, P. M. and Keller, C. P.: Multivariate interpolation to incorporate thematic surface data using inverse distance weighting (IDW), Comput. Geosci., 22, 795-799, doi: 10.1016/0098-3004(96)00021-0, 1996.
340 Bashmachnikov, I., Boutov, D., and Dias, J.: Manifestation of two meddies in altimetry and sea-surface temperature, Ocean Science, 9, 249-259, doi: 10.5194/os-9-249-2013, 2013.
Bashmachnikov, I., Carton, X., and Belonenko, T.: Characteristics of surface signatures of Mediterranean water eddies, J. Geophys. Res. Oceans, 119, 7245-7266, doi: 10.1002/2014JC010244, 2014.
Bôas, A. B. V., Sato, O. T., Chaigneau, A., and Castelão, G. P.: The signature of mesoscale eddies on the air-sea turbulent
345 heat fluxes in the South Atlantic Ocean, Geophys. Res. Lett., 42, 1856–1862, doi: 10.1002/2015GL063105, 2015.

Brock, J. C., McClain, C. R., Luther, M. E., and Hay, W. W.: The phytoplankton bloom in the northwestern Arabian Sea during the southwest monsoon of 1979, J. Geophys. Res. Oceans, 96, 20623-20642, doi: 10.1029/91JC01711, 1991.

Caballero, A., Pascual, A., Dibarboure, G., and Espino, M.: Sea level and Eddy Kinetic Energy variability in the Bay of Biscay, inferred from satellite altimeter data, Journal of Marine Systems, 72, 116-134, doi: 10.1016/j.jmarsys.2007.03.011, 2008.

Chaigneau, A., Le Texier, M., Eldin, G., Grados, C., and Pizarro, O.: Vertical structure of mesoscale eddies in the eastern South Pacific Ocean: A composite analysis from altimetry and Argo profiling floats, J. Geophys. Res. Oceans, 116, C12033, doi: 10.1029/2011jc007134, 2011.

Chelton, D. B., Schlax, M. G., and Samelson, R. M.: Global observations of nonlinear mesoscale eddies, Prog. Oceanogr., 91, 167–216, doi: 10.1016/j.pocean.2011.01.002, 2011a.

Chelton, D. B., Gaube, P., Schlax, M. G., Early, J. J., and Samelson, R. M.: The influence of nonlinear mesoscale eddies on near-surface oceanic chlorophyll, Science, 334, 328-332, doi: 10.1126/science.1208897, 2011b.

Chen, G., Han, G., and Yang, X.: On the intrinsic shape of oceanic eddies derived from satellite altimetry, Remote Sens. Environ., 228, 75-89, doi: 10.1016/j.rse.2019.04.011, 2019.

Chen, G., Wang, D., and Hou, Y.: The features and interannual variability mechanism of mesoscale eddies in the Bay of Bengal, Cont. Shelf Res., 47, 178-185, doi: 10.1016/j.csr.2012.07.011, 2012.

Cheng, X., McCreary, J. P., Qiu, B., Qi, Y., Du, Y., and Chen, X.: Dynamics of Eddy Generation in the Central Bay of Bengal, J. Geophys. Res. Oceans, 123, 6861-6875, doi: 10.1029/2018jc014100, 2018.

Cui, W., Yang, J., and Ma, Y.: A statistical analysis of mesoscale eddies in the Bay of Bengal from 22–year altimetry data, Acta Oceanol. Sin., 35, 16-27, doi: 10.1007/s13131-016-0945-3, 2016.

Dolz, J., Gopinath, K., Yuan, J., Lombaert, H., Desrosiers, C., and Ayed, I. B.: HyperDense-Net: A hyper-densely connected CNN for multi-modal image segmentation, IEEE Trans. Med. Imaging, 38, 1116-1126, doi: 10.1109/TMI.2018.2878669, 2018.

Findlater, J.: A major low-level air current near the Indian Ocean during the northern summer, Q. J. Roy. Meteor. Soc., 95, 362-380, doi: 10.1002/qj.49709540409, 1969.

Gaube, P., Chelton, D. B., Strutton, P. G., and Behrenfeld, M. J.: Satellite observations of chlorophyll, phytoplankton biomass, and Ekman pumping in nonlinear mesoscale eddies, J. Geophys. Res. Oceans, 118, 6349-6370, doi: 10.1002/2013jc009027, 2013.

Gaube, P., McGillicuddy, D. J., Chelton, D. B., Behrenfeld, M. J., and Strutton, P. G.: Regional variations in the influence of mesoscale eddies on near-surface chlorophyll, J. Geophys. Res. Oceans, 119, doi: 10.1016/j.rse.2007.03.012, 2014.

Greaser, S. R., Subrahmanyam, B., Trott, C. B., and Roman-Stork, H. L.: Interactions between mesoscale eddies and synoptic oscillations in the Bay of Bengal during the strong monsoon of 2019, J. Geophys. Res. Oceans, 125, e2020JC016772, doi: 10.1029/2020JC016772, 2020.

Gulakaram, V. S., Vissa, N. K., and Bhaskaran, P. K.: Characteristics and vertical structure of oceanic mesoscale eddies in the Bay of Bengal, Dyn. Atmospheres Oceans, 89, doi: 10.1016/j.dynatmoce.2020.101131, 2020.

Ham, Y. G., Kim, J. H., and Luo, J. J.: Deep learning for multi-year ENSO forecasts, Nature, 573, 568-572, doi: 10.1038/s41586-019-1559-7, 2019.

Hsu, P.-C., Lin, C.-C., Huang, S.-J., and Ho, C.-R.: Effects of Cold Eddy on Kuroshio Meander and Its Surface Properties, East of Taiwan, IEEE J. Sel. Top. Appl. Earth Obs. Remote Sens., 9, 5055-5063, doi: 10.1109/jstars.2016.2524698, 2016.

Jiang, H., Song, Y., Mironov, A., Yang, Z., Xu, Y., and Liu, J.: Accurate mean wave period from SWIM instrument onboard CFOSAT, Remote Sens. Environ., 280, 113149, doi: 10.1016/j.rse.2022.113149, 2022.

Klemas, V. and Yan, X.-H.: Subsurface and deeper ocean remote sensing from satellites: An overview and new results, Prog. Oceanogr., 122, 1-9, doi: 10.1016/j.pocean.2013.11.010, 2014.

Kumar, S. P., Madhupratap, M., Kumar, M. D., Muraleedharan, P., De Souza, S., Gauns, M., and Sarma, V.: High biological productivity in the central Arabian Sea during the summer monsoon driven by Ekman pumping and lateral advection, Current Science, 1633-1638, doi, 2001.

Kumar, S. P., Muraleedharan, P. M., Prasad, T. G., Gauns, M., Ramaiah, N., de Souza, S. N., Sardesai, S., and Madhupratap, M.: Why is the Bay of Bengal less productive during summer monsoon compared to the Arabian Sea?, Geophys. Res. Lett., 29, doi: 10.1029/2002gl016013, 2002.

Lecun, Y., Bengio, Y., and Hinton, G. E.: Deep learning, Nature, 521, 436-444, doi: 10.1038/nature14539, 2015.

Lee, C. M., Jones, B. H., Brink, K. H., and Fischer, A. S.: The upper-ocean response to monsoonal forcing in the Arabian Sea: seasonal and spatial variability, Deep-Sea Research Part II, 47, 1177-1226, doi: 10.1016/S0967-0645(99)00141-1, 2000.

Lehahn, Y., d'Ovidio, F., Levy, M., Amitai, Y., and Heifetz, E.: Long range transport of a quasi isolated chlorophyll patch by an Agulhas ring, Geophys. Res. Lett., 38, doi: 10.1029/2011gl048588, 2011.

400 Liu, Y., Chen, G., Sun, M., Liu, S., and Tian, F.: A parallel SLA-based algorithm for global mesoscale eddy identification, Journal of Atmospheric and Oceanic Technology, 33, 2743–2754, doi: 10.1175/JTECH-D-16-0033.1, 2016.

Lu, W., Su, H., Yang, X., and Yan, X.-H.: Subsurface temperature estimation from remote sensing data using a clustering-neural network method, Remote Sens. Environ., 229, 213-222, doi: 10.1016/j.rse.2019.04.009, 2019.

Maritorena, S., d'Andon, O. H. F., Mangin, A., and Siegel, D. A.: Merged satellite ocean color data products using a bio-
405 optical model: Characteristics, benefits and issues, Remote Sens. Environ., 114, 1791-1804, doi: 10.1016/j.rse.2010.04.002, 2010.

Mcdougall, T. J. and Barker, P. M.: Getting started with TEOS-10 and the Gibbs Seawater (GSW) Oceanographic Toolbox, SCOR/ IAPSO WG, 127, 1–28, doi, 2011.

Morales, C. E., Hormazabal, S., Correa-Ramirez, M., Pizarro, O., Silva, N., Fernandez, C., Anabalón, V., and Torreblanca,
410 M. L.: Mesoscale variability and nutrient–phytoplankton distributions off central-southern Chile during the upwelling season: The influence of mesoscale eddies, Prog. Oceanogr., 104, 17-29, doi: 10.1016/j.pocean.2012.04.015, 2012.

Piontkovski, S., Al-Azri, A., and Al-Hashmi, K.: Seasonal and interannual variability of chlorophyll-a in the Gulf of Oman compared to the open Arabian Sea regions, Int. J. Remote Sens., 32, 7703-7715, doi: 10.1080/01431161.2010.527393, 2011.

Prasad, T. G.: A comparison of mixed-layer dynamics between the Arabian Sea and Bay of Bengal: One-dimensional model
415 results, J. Geophys. Res. Oceans, 109, doi: 10.1029/2003jc002000, 2004.

Pujol, M.-I., Faugère, Y., Taburet, G., Dupuy, S., Pelloquin, C., Ablain, M., and Picot, N.: DUACS DT2014: the new multi-mission altimeter data set reprocessed over 20 years, Ocean Science, 12, 1067–1090, doi: 10.5194/os-12-1067-2016, 2016.

Reynolds, R. W., Smith, T. M., Liu, C., Chelton, D. B., Casey, K. S., and Schlax, M. G.: Daily high-resolution-blended analyses for sea surface temperature, J. Clim., 20, 5473–5496, doi: 10.1175/2007JCLI1824.1, 2007.

420 Ronneberger, O., Fischer, P., and Brox, T.: U-Net: Convolutional Networks for Biomedical Image Segmentation, Cham, 234-241,

Shafeeque, M., Balchand, A. N., Shah, P., George, G., B. R, S., Varghese, E., Joseph, A. K., Sathyendranath, S., and Platt, T.: Spatio-temporal variability of chlorophyll-a in response to coastal upwelling and mesoscale eddies in the South Eastern Arabian Sea, Int. J. Remote Sens., 42, 4836-4863, doi: 10.1080/01431161.2021.1899329, 2021.

425 Siegel, D. A., Peterson, P., McGillicuddy, D. J., Maritorena, S., and Nelson, N. B.: Bio-optical footprints created by mesoscale eddies in the Sargasso Sea, Geophys. Res. Lett., 38, n/a-n/a, doi: 10.1029/2011gl047660, 2011.

Smitha, B., Sanjeevan, V., Padmakumar, K., Hussain, M. S., Salini, T., and Lix, J.: Role of mesoscale eddies in the sustenance of high biological productivity in North Eastern Arabian Sea during the winter-spring transition period, Sci. Total Environ., 809, 151173, doi: 10.1016/j.scitotenv.2021.151173, 2022.

430 Somayajulu, Y. K., Murty, V. S. N., and Sarma, Y. V. B.: Seasonal and inter-annual variability of surface circulation in the Bay of Bengal from TOPEX/Poseidon altimetry, Deep Sea Res. Part II Top. Stud. Oceanogr., 50, 867-880, doi: 10.1016/S0967-0645(02)00610-0, 2003.

Su, H., Wu, X., Yan, X.-H., and Kidwell, A.: Estimation of subsurface temperature anomaly in the Indian Ocean during recent global surface warming hiatus from satellite measurements: A support vector machine approach, Remote Sens.
435 Environ., 160, 63-71, doi: 10.1016/j.rse.2015.01.001, 2015.

Su, H., Zhang, T., Lin, M., Lu, W., and Yan, X.-H.: Predicting subsurface thermohaline structure from remote sensing data based on long short-term memory neural networks, Remote Sens. Environ., 260, doi: 10.1016/j.rse.2021.112465, 2021.

Trott, C. B., Subrahmanyam, B., Chaigneau, A., and Delcroix, T.: Eddy tracking in the northwestern Indian Ocean during southwest monsoon regimes, Geophys. Res. Lett., 45, 6594-6603, doi: 10.1029/2018gl078381, 2018.

440 Trott, C. B., Subrahmanyam, B., Chaigneau, A., and Roman-Stork, H. L.: Eddy-induced temperature and salinity variability in the Arabian Sea, Geophys. Res. Lett., doi: 10.1029/2018GL081605, 2019.

Wang, Z.-F., Sun, L., Li, Q.-Y., and Cheng, H.: Two typical merging events of oceanic mesoscale anticyclonic eddies, Ocean Science, 15, 1545-1559, doi: 10.5194/os-15-1545-2019, 2019.

Yang, X., Xu, G., Liu, Y., Sun, W., Xia, C., and Dong, C.: Multi-Source Data Analysis of Mesoscale Eddies and Their
445 Effects on Surface Chlorophyll in the Bay of Bengal, Remote Sens., 12, doi: 10.3390/rs12213485, 2020.

Zhan, P., Guo, D., and Hoteit, I.: Eddy-induced transport and kinetic energy budget in the Arabian Sea, Geophys. Res. Lett., 47, doi: 10.1029/2020GL090490, 2020.

Zhang, Z., Zhang, Y., and Wang, W.: Three-compartment structure of subsurface-intensified mesoscale eddies in the ocean, J. Geophys. Res. Oceans, 122, 1653-1664, doi: 10.1002/2016jc012376, 2017.

450 Zhang, Z., Qiu, B., Klein, P., and Travis, S.: The influence of geostrophic strain on oceanic ageostrophic motion and surface chlorophyll, Nat Commun, 10, 2838, doi: 10.1038/s41467-019-10883-w, 2019.

Table 1. Composite extremum values ±1 Confidence Interval (CI) for SSTA/Chl-a' over four kinds of eddies. The CI was computed at the location of SSTA/Chl-a' extremum in composite maps.

		AS		BoB	
		Summer	Winter	Summer	Winter
SSTA (°C)	SAEs	0.14±0.004	0.08±0.002	0.09±0.003	0.08±0.003
	SSAEs	-0.12±0.004	-0.07±0.002	-0.10±0.004	-0.09±0.003
	SCEs	-0.16±0.004	-0.10±0.002	-0.11±0.004	-0.10±0.003
	SSCEs	0.14±0.004	0.05±0.002	0.09±0.003	0.08±0.003
Chl-a' (mg/m³)	SAEs	-0.040±0.004	-0.048±0.005	-0.029±0.004	-0.018±0.002
	SSAEs	-0.019±0.004	-0.017±0.002	-0.023±0.003	0.022±0.004
	SCEs	0.074±0.007	0.084±0.005	0.022±0.006	0.033±0.004
	SSCEs	0.019±0.003	0.040±0.007	0.016±0.005	0.008±0.003
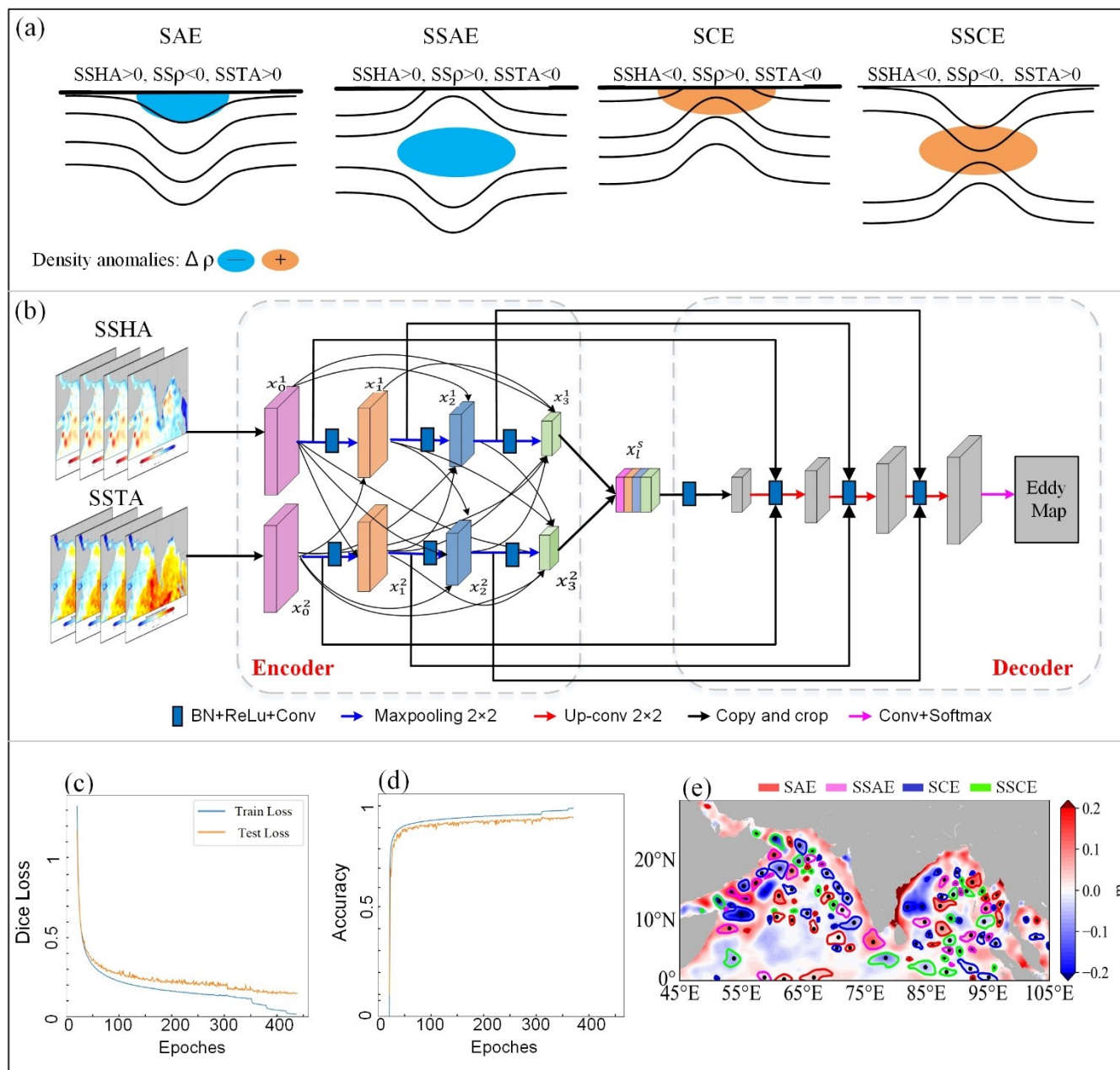
Figure 1. (a) Isopycnal displacements, SSHA, and SSTA for SAE, SSAE, SCE, and SSCE. (b) Flow chart of the DL-based eddy identification model. Loss (c) and accuracy (d) curves produced by the DL-based eddy identification model. (e) SSCEs, SCEs, SAEs, and SSAEs detected by the DL-based model on December 1, 2005.
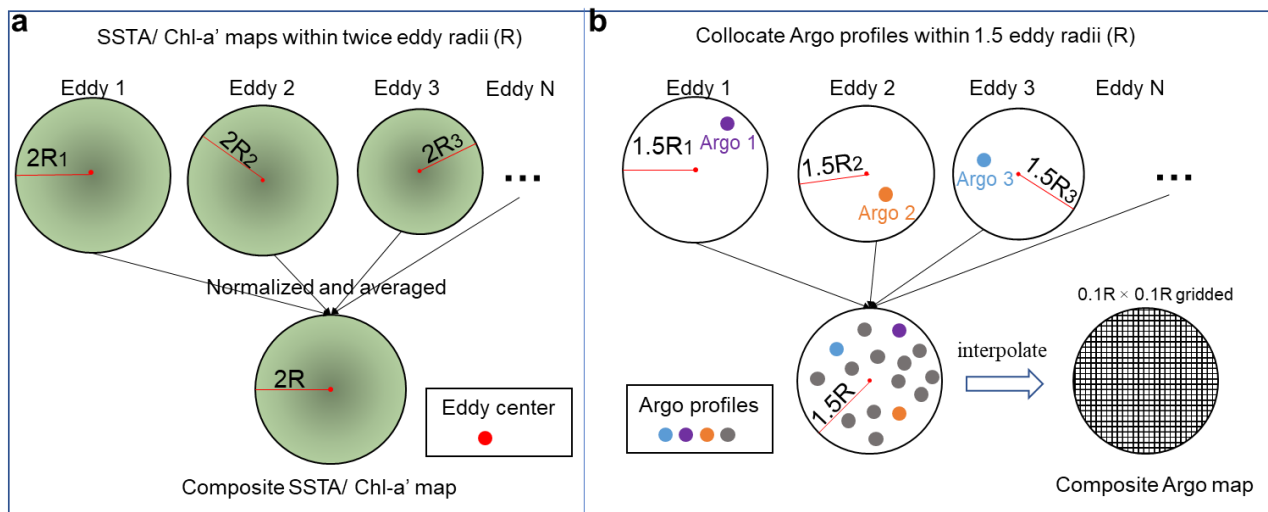
460   **Figure 2.** Schematic of composite analysis of SST, Chl-a (a), and Argo profiles (b) for eddies.
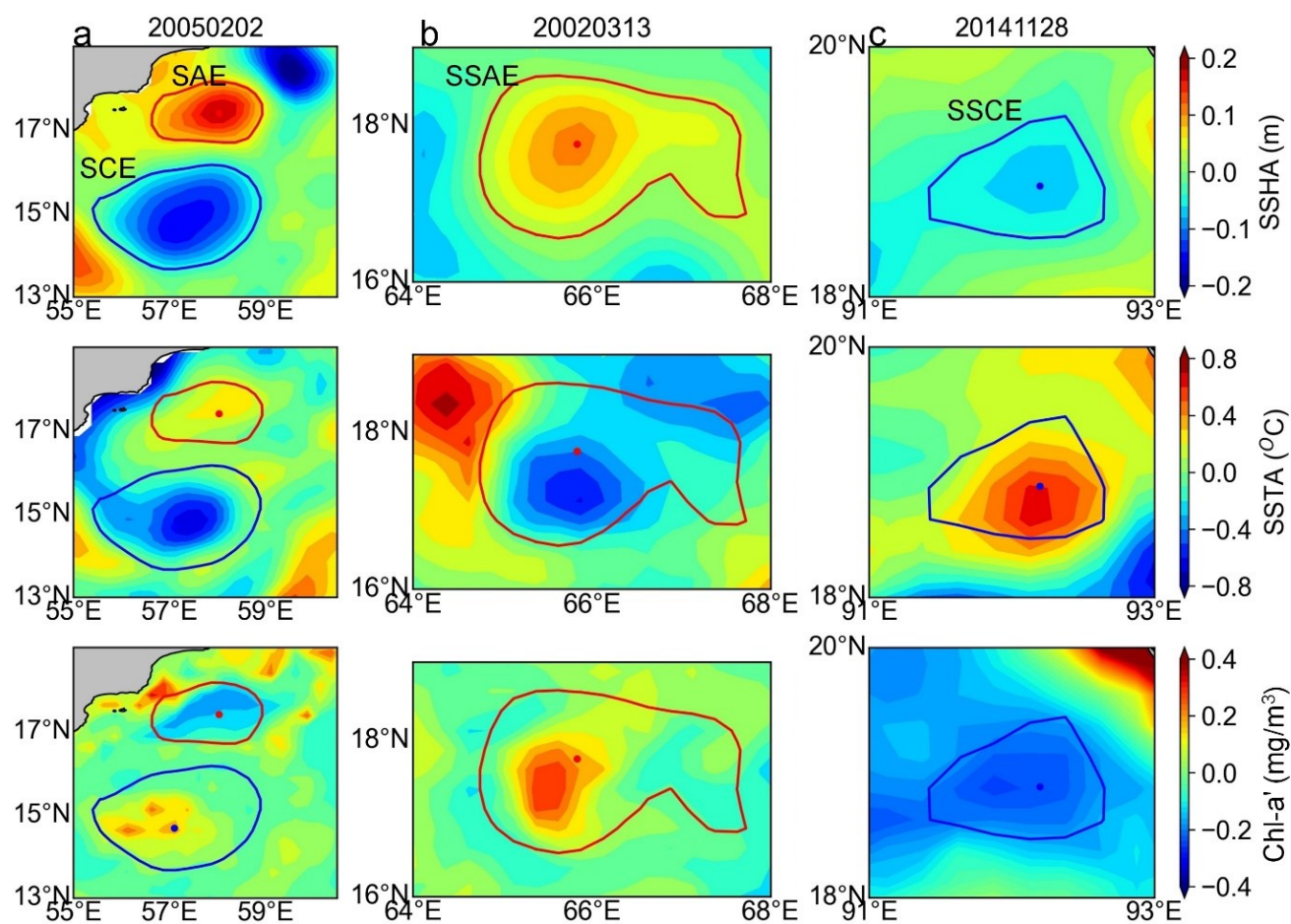
Figure 3. Case study of eddy imprints on SSHA, SSTA, and Chl-a' maps for an SAE and an SCE (a), an SSAE (b), and an SSCE (c). Red and blue lines denote eddy edges.

465
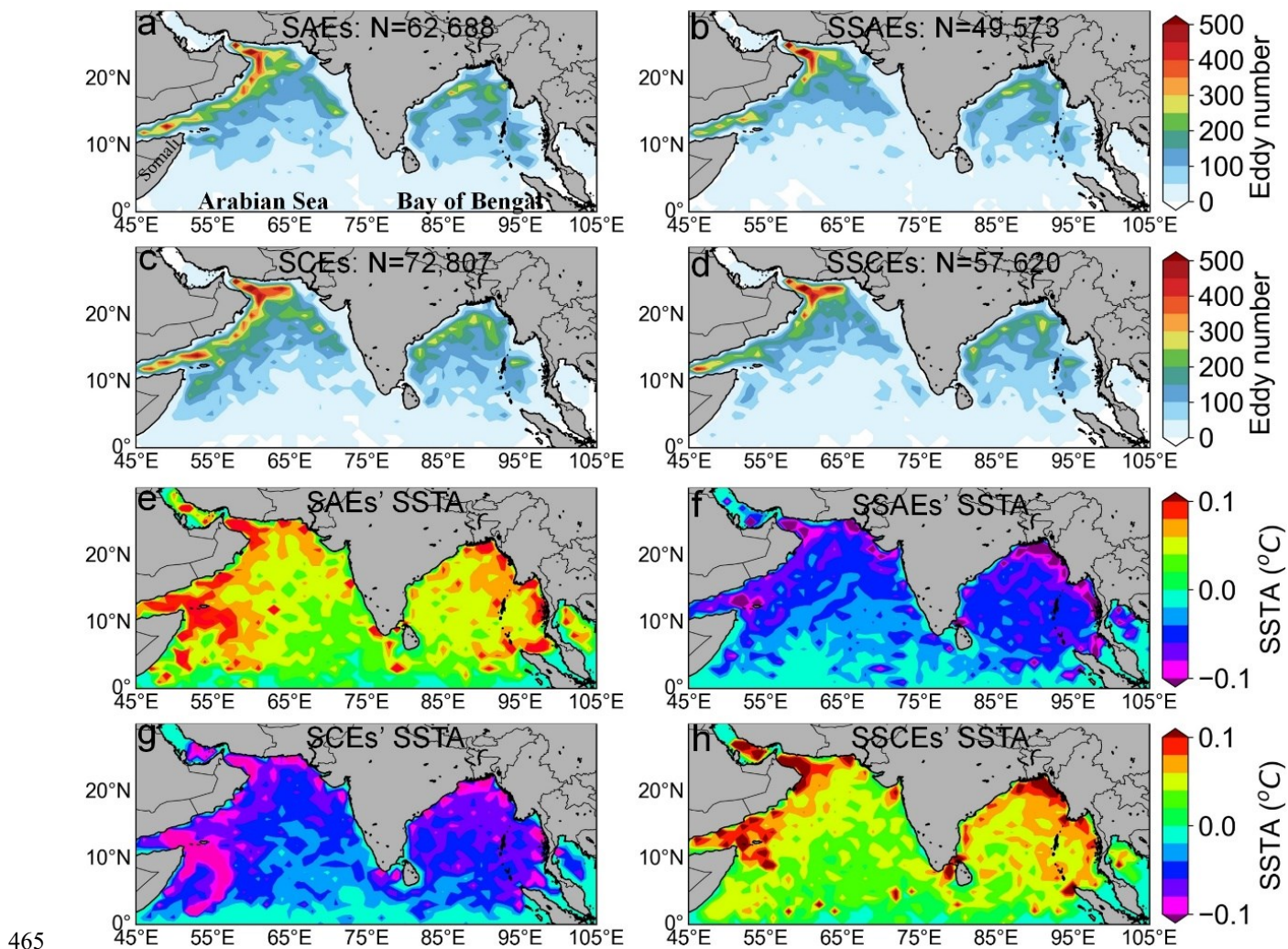
Figure 4. The spatial distribution of eddy concentration (a-d) and SSTA (e-h) within SAEs, SSAEs, SCEs, and SSCEs. N is the sum of eddies of the same kind observed in the NIO during 2000-2015.
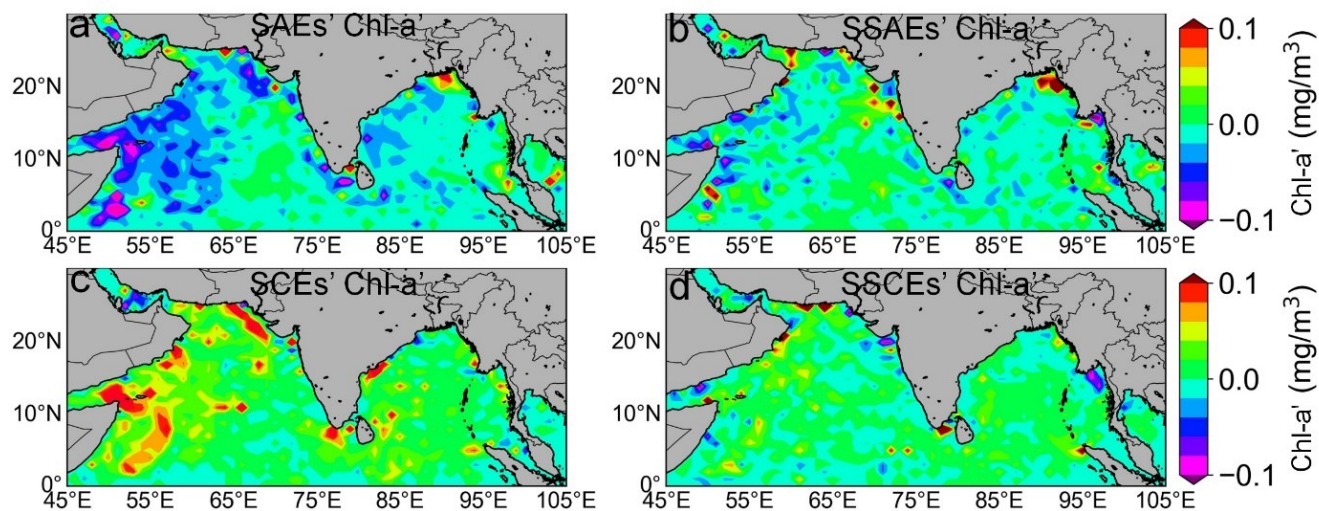
Figure 5. Spatial distribution of eddy-induced Chl-a' for SAEs (a), SSAEs (b), SCEs (c), and SSCEs (d) in the NIO during 2000-2015.
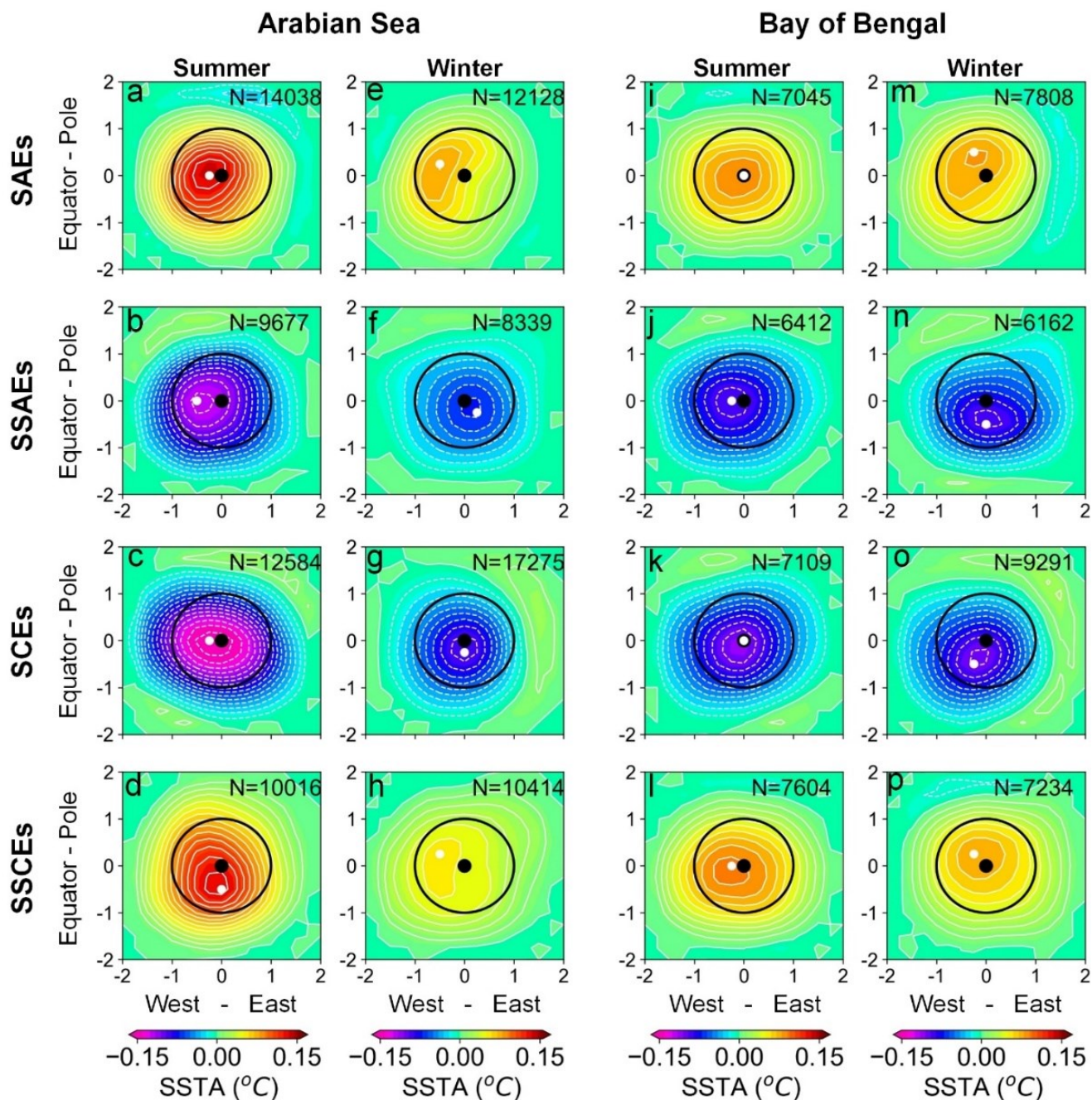
Figure 6. Composite SSTA over SAEs, SSAEs, SCEs, and SSCEs in the AS (a-d, i-l) and BoB (e-h, m-p), respectively. Black points denote eddy centers, while white points represent SSTA extremum locations. N is the sum of eddies of the same kind during 2000-2015.

475
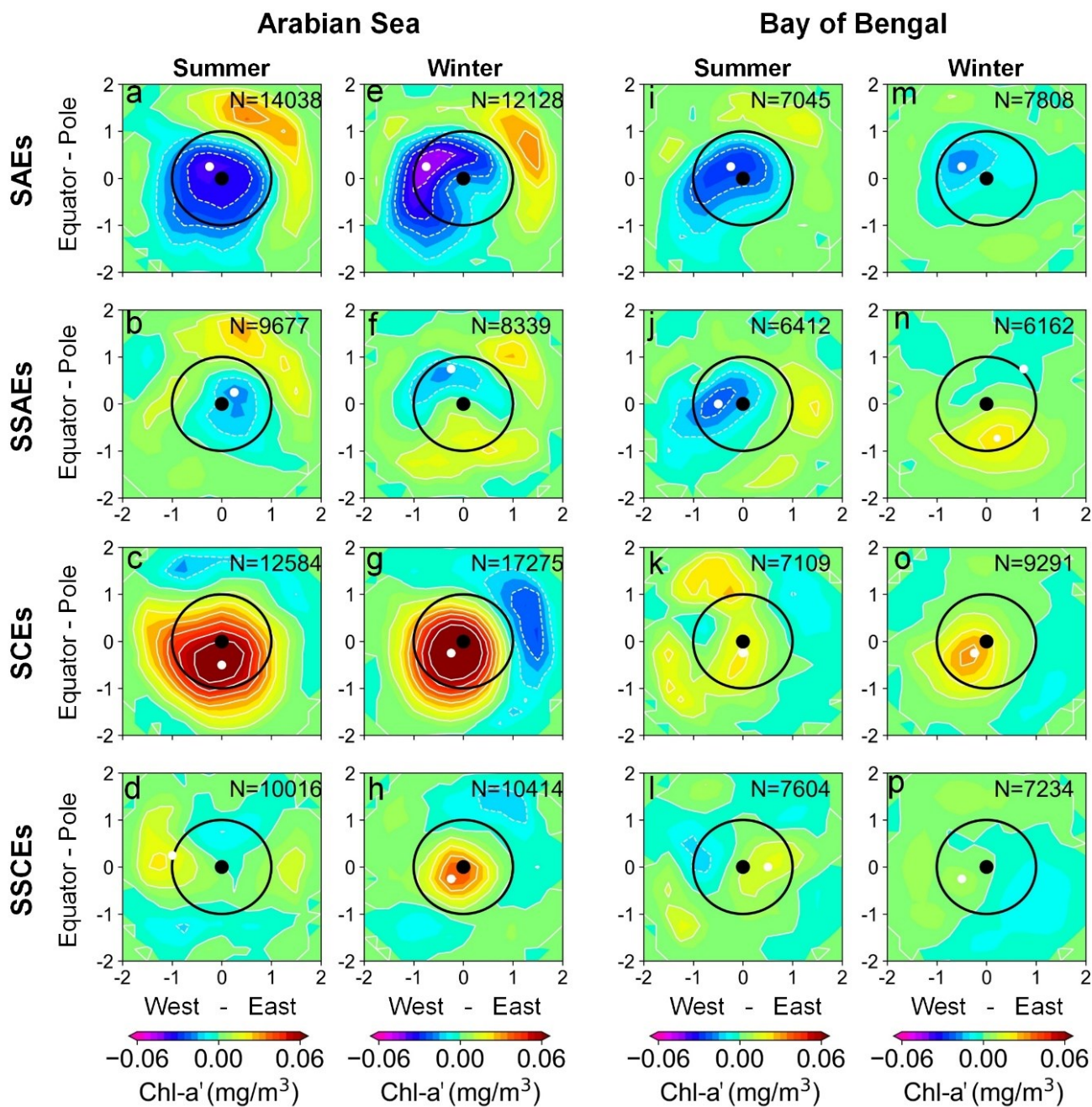
Figure 7. Composite Chl-a' over SAEs, SSAEs, SCEs, and SSCEs in the AS (a-d, i-l) and BoB (e-h, m-p), respectively. Black points denote eddy centers, while white points represent Chl-a' extremum locations. N is the sum of eddies of the same kind during 2000-2015.
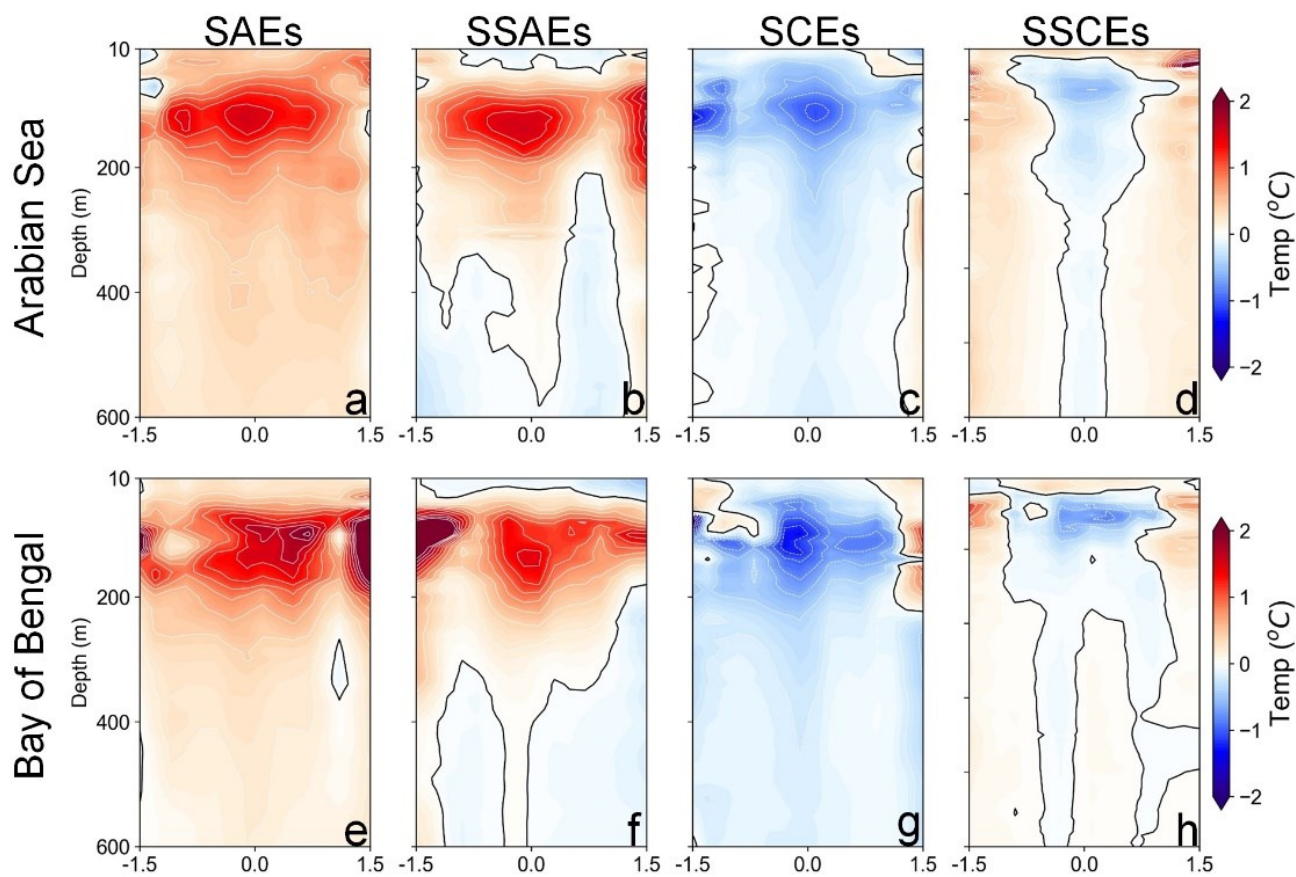
Figure 8. Composite zonal sections of the vertical temperature structure within SAEs, SSAEs, SCEs, and SSCEs in the AS (a-d) and the BoB (e-h) during 2000-2015. Black lines denote contours in 0°C.
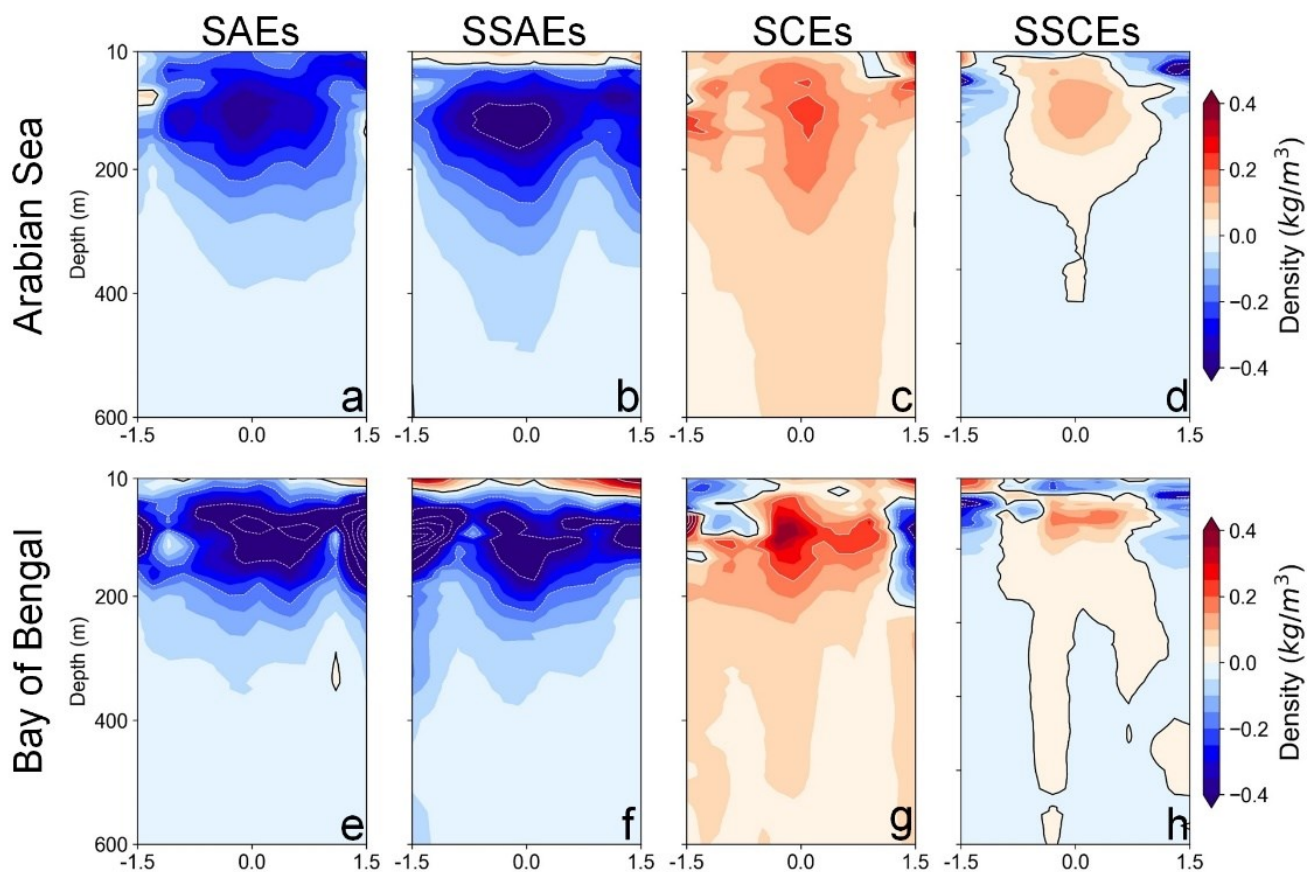
Figure 9. Composite zonal sections of the vertical potential density structure within SAEs, SSAEs, SCEs, and SSCEs in the AS (a-d) and
the BoB (e-h) from 2000-2015. Black lines denote potential density in 0 kg/m^3.